The Journal of Chemical Physics ARTICLE pubs.aip.org/aip/jcp

Multiscale modeling of charge transfer in hole-transporting materials: Linking molecular morphology to charge mobility

Cite as: J. Chem. Phys. 162, 184702 (2025); doi: 10.1063/5.0265890
Submitted: 16 February 2025 • Accepted: 22 April 2025 •
Published Online: 8 May 2025

Sanyam and Anirban Mondal[a)]

AFFILIATIONS

Department of Chemistry, Indian Institute of Technology Gandhinagar, Gujarat 382355, India

[a)]Author to whom correspondence should be addressed: amondal@iitgn.ac.in

ABSTRACT

Hole-transporting materials (HTMs) play a pivotal role in the performance and stability of organic electronic devices by enabling efficient hole transport. This study employs a multiscale approach to explore the relationship between molecular morphology and charge transfer properties in four HTM molecules. By combining quantum mechanical calculations, molecular dynamics simulations, and kinetic Monte Carlo modeling, we analyze key structural features such as radial distribution functions, principal axis orientations, and non-covalent interactions. Our findings reveal that molecular size and substituent effects significantly influence non-covalent interactions and molecular alignments, thereby affecting charge transport pathways. Charge transfer rates and energetic disorder were modeled using the master equation, and mobilities were computed, showing satisfactory agreement with experimental data. This comprehensive analysis provides valuable insights into the design of HTMs for organic electronic devices, emphasizing the importance of molecular architecture in optimizing charge mobility and minimizing energy losses.

I. INTRODUCTION

The advancement of organic electronic devices, such as organic light-emitting diodes (OLEDs) and organic–inorganic perovskite solar cells, critically depends on efficient hole-transporting materials (HTMs).[1–4] HTMs serve a dual function: facilitating hole transport from the anode to the active layer while blocking electrons, thereby enhancing charge separation and transport within the device. For optimal performance, HTMs must possess well-aligned ionization energies (IE) relative to the active layer and sufficiently high electron affinities (EA) to mitigate exciton quenching.[5] Beyond energy alignment, charge carrier mobility is a key determinant of device efficiency, influencing parameters such as turn-on voltage in OLEDs and charge extraction rates in solar cells.[6–8] These properties are strongly influenced by molecular packing and non-covalent interactions, highlighting the necessity of detailed structure-property relationship analyses for designing next-generation HTMs.

Previous studies have demonstrated that molecular architecture—such as the incorporation of diphenylamine, carbazole, or spiro-configured motifs—plays a crucial role in determining the charge transport properties and stability of HTMs.[9–11] For example, the widely used HTM 4,4′-bis[N-(1-naphthyl)-N-phenylamino]biphenyl (NPB) exemplifies how structural modifications can optimize charge mobility and energy alignment.[12,13] While tailoring molecular structures, such as introducing branched or fluorene-based frameworks, has proven effective in improving HTM performance, a fundamental challenge remains in linking molecular packing and non-covalent interactions to charge transport efficiency.[14–20] Understanding these microscopic interactions is essential for developing a rational design strategy for efficient and stable HTMs.

Computational methods, particularly multiscale simulations, provide powerful tools for exploring these complex structure-property relationships.[21] While gas-phase quantum mechanical (QM) calculations offer insights into molecular properties such as ionization energies and reorganization energies, they do not account for bulk electrostatic and polarization effects that critically influence charge transport.[21–23] Consequently, bulk-phase molecular dynamics (MD) simulations are essential for capturing realistic morphological features and intermolecular interaction networks.

However, classical force fields often lack sufficient accuracy in parameterizing dihedral flexibility and non-covalent interactions, necessitating careful optimization to ensure physically meaningful morphologies.[19,24] Even with optimized morphologies, MD simulations alone cannot capture electronic structure details, requiring a multiscale approach[25–28] that integrates molecular morphologies with quantum mechanical calculations and kinetic Monte Carlo (kMC) simulations. The VOTCA framework[29,30] enables such an approach by combining MD morphologies with electronic structure calculations to predict charge transport properties.

In this study, we employ a multiscale simulation framework to elucidate the relationship between molecular morphology and charge transport in HTMs. QM calculations are first used to determine fundamental gas-phase properties, including ionization energies, electron affinities, and reorganization energies. We then refine force field parameters to accurately describe intermolecular interactions, which are used to generate amorphous morphologies via MD simulations. These morphologies are analyzed using radial distribution functions, principal axis orientations, and reduced density gradient (RDG) analysis to characterize molecular packing and non-covalent interactions. Bulk-modified ionization energies and site energy distributions are subsequently computed, providing insights into energetic disorder and electronic coupling. Finally, charge transport is modeled using kMC simulations to track hole diffusion within the amorphous HTM morphologies.

A key aspect of this study is the comparison between simulated and experimental charge mobilities. The computed mobilities, derived from amorphous morphologies, are an order of magnitude lower than experimental values. This discrepancy arises primarily from morphological differences: experimentally fabricated HTM films often exhibit partial crystallinity and lower energetic disorder, whereas our simulations focus exclusively on amorphous phases. While a crystalline morphology would likely yield higher simulated mobilities, such an approach requires an experimentally validated crystal structure, which is currently unavailable. More importantly, amorphous morphologies are particularly relevant to OLED device architectures, where HTM layers typically exhibit significant disorder. Therefore, our emphasis is not on the exact reproduction of experimental mobility values but rather on elucidating the molecular interactions and structural motifs that govern charge transport in amorphous HTMs. By establishing these fundamental structure–property relationships, this work provides insights to inform the rational design of future HTMs for organic electronic and hybrid devices.

II. METHODS

We investigated four hole-transporting materials labeled DD, DF, DN, and DP, each depicted in Fig. 1. The experimental synthesis and characterization of these molecules are reported in Ref. 31. These HTMs consist of five distinct molecular fragments. Three of these fragments—FL, AT, and HE—are common across all molecules, with structural variations limited to the peripheral fragments labeled LB and RB. Specifically, the DF and DP molecules are structurally identical except for two fluorine (F) atoms substituted onto the peripheral phenyl rings in DF's LB and RB fragments. In contrast, DN incorporates naphthalene units at the peripheral positions, while DD features N, N, N-triphenyl groups as its side fragments.

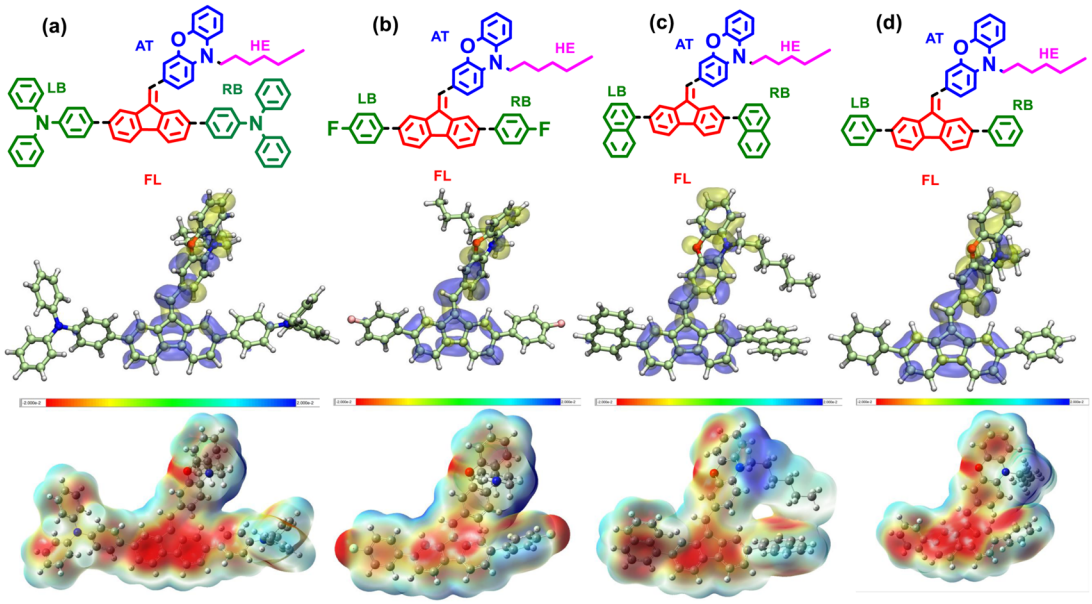

FIG. 1. The chemical structures of the four investigated molecules: (a) DD, (b) DF, (c) DN, and (d) DP. Each molecule has five fragments: FL, LB, RB, AT, and HE. The second and third rows depict frontier molecular orbitals and the electrostatic potential maps of each molecule [isovalue: −0.02 atomic unit (minimum) to +0.02 atomic unit (maximum)]. Yellow and blue lobes represent HOMO and LUMO in the middle row, respectively.

A. Quantum mechanical calculations

All quantum mechanical calculations were performed using the Gaussian09 software package.[32] Gas-phase electronic properties, including ionization energy and electron affinity, were calculated with density functional theory (DFT) using the B3LYP functional and the 6-311+G(d, p) basis set. The ionization energy and electron affinity were calculated as follows:

$$\mathrm{IE} = E_{\mathrm{cC}} - E_{\mathrm{nN}}, \tag{1}$$

$$\mathrm{EA} = E_{\mathrm{nN}} - E_{\mathrm{aA}}, \tag{2}$$

where E_{cC} is the energy of the optimized cationic geometry, E_{aA} is the energy of the anionic geometry, and E_{nN} is the energy of the optimized neutral molecule.

The reorganization energy, essential for understanding charge transfer, accounts for the charging and discharging of a molecule. This includes the intramolecular reorganization energy ($\lambda_{ij}^{\mathrm{int}}$), attributed to the internal structural adjustment of the molecules involved, and the intermolecular or outer-sphere component ($\lambda_{ij}^{\mathrm{out}}$), which results from the relaxation of the surrounding environment. Only intramolecular reorganization energy is considered here due to the minimal impact of the outer-sphere contribution in amorphous solids, where the Pekar factor is ~0.01.[30] The intramolecular component is calculated as

$$\lambda_{ij}^{\mathrm{int}} = \left(U_i^{\mathrm{nC}} - U_i^{\mathrm{nN}}\right) + \left(U_j^{\mathrm{cN}} - U_j^{\mathrm{cC}}\right), \tag{3}$$

$$\lambda_{ij}^{\mathrm{int}} = \left(U_i^{\mathrm{nA}} - U_i^{\mathrm{nN}}\right) + \left(U_j^{\mathrm{aN}} - U_j^{\mathrm{aA}}\right), \tag{4}$$

In these equations, lowercase letters denote the molecular charge state—neutral (n), cation (c), or anion (a)—while uppercase letters indicate the geometry—neutral (N), cationic (C), or anionic (A).

B. Molecular dynamics simulations

Accurate force field parameters are essential for reliably predicting amorphous morphologies and charge transport properties in molecular systems. To achieve this, frequency calculations were initially performed on the optimized ground-state geometries of each compound, serving as the basis for parameter generation. Lennard-Jones (LJ) and bonded parameters were derived using the Sobtop program,[33] which processed the frequency outputs to establish the force field parameters. This approach was demonstrated to yield accurate all-atom potential parameters for organic molecules.[34–36] In addition, atomic partial charges were determined with the density-derived electrostatic and chemical (DDEC) scheme,[37] employing the same functional and basis set used in our DFT calculations for consistency.

Molecular dynamics simulations, carried out in GROMACS,[38,39] were then used to model amorphous morphologies. A controlled annealing procedure—consisting of sequential heating and cooling steps—was implemented to generate these amorphous configurations.[21,22] To generate the initial configuration, 1000 molecules were packed into a cubic box with dimensions $15 \times 15 \times 15$ nm^3 using Packmol.[40] Energy minimization was then executed via the steepest descent method to relieve any initial steric clashes. The system was equilibrated in two stages: heating and cooling. During the heating phase, the temperature was increased from 100 to 300 K over 0.3 ns, followed by a further increase to 800 K over 1.2 ns. The system was maintained at 800 K for an additional 1.5 ns to ensure thorough mixing. In the cooling phase, the temperature was reduced from 800 to 600 K over 0.2 ns and further to 300 K over 0.8 ns. The system was then equilibrated at 300 K for 2.0 ns. Finally, a 15 ns production trajectory was generated for analysis. All MD simulations were conducted in the NPT ensemble, with temperature and pressure control achieved through a canonical velocity rescaling thermostat[41] and a Berendsen barostat.[42] To accurately account for long-range electrostatic interactions, the particle mesh Ewald (PME) method[43] was employed, with a time step of 1 femtosecond for integrating the equations of motion. The density stabilized during both equilibration stages, with the simulation box dimensions reducing from 15 to ~11 nm during the heating phase and further by ~0.5 nm during the cooling phase. This contraction indicates that the molecules were not constrained by the initial configuration and rearranged naturally during equilibration. The morphology was validated by comparing dipole moments derived from MD and QM calculations and through structural comparisons (*vide infra*), confirming the robustness of the generated morphologies.

C. Non-covalent interactions

The trajectories obtained from MD simulations were visualized with the help of VMD software.[44] The characterization and identification of non-covalent interaction regions were made with the help of the NCIPLOT4 package.[45,46] This tool effectively detects weak interaction regions by analyzing the electron density, $\rho(r)$, and its derivatives, identifying critical points indicative of non-covalent interactions. The reduced density gradient (RDG), which highlights these regions, is defined by

$$\mathrm{RDG}(r) = \frac{1}{2(3\pi^2)^{1/3}} \frac{|\nabla\rho(r)|}{\rho^{4/3}(r)}. \tag{5}$$

The RDG is highly sensitive to low-density regions, approaching zero at critical points where the electron density gradient, $\nabla\rho(r)$, becomes dominant. This method uses promolecular electron density estimates, avoiding the computational expense of self-consistent field (SCF) methods while maintaining accuracy for large systems.

D. Density of states

The amorphous morphologies generated from MD simulations served as the basis for calculating site energies through a perturbative approach. This approach involves determining total site energy by adding the electrostatic and induction contributions to the gas-phase ionization energy (IE_0) or electron affinity (EA_0). The electrostatic term was computed via Coulomb summation, using distributed multipoles obtained from the GDMA program[47] for neutral and charged states in their ground-state configurations. For polarization effects, a polarizable force field following the Thole model[48,49] was applied, relying on isotropic atomic polarizabilities (α_{ai}) specific to atom a in molecule i. To enhance accuracy in site energy calculations, the aperiodic embedding of charges method was employed as implemented in the VOTCA package.[29,30]

E. Coupling elements and mobilities

Due to the amorphous nature of the organic molecules, the charge carriers follow the hopping mechanism and possess weak coupling and high energetic disorder due to the different site energies present within the system.[21] The hopping of the carriers is an endothermic process and can be thermally activated. The rate of charge transfer was calculated from the semi-classical Marcus equation,[50–52]

$$\omega_{ij} = \frac{2\pi}{\hbar} J_{ij}^2 \sqrt{\frac{1}{4\pi\lambda_{ij} k_B T}} \exp\left(\frac{-(\Delta E_{ij} - \lambda_{ij})^2}{4\lambda_{ij} k_B T}\right), \quad (6)$$

where T is the temperature, k_B is Boltzmann's constant, λ_{ij} is the reorganization energy, J_{ij} is the electronic coupling matrix element, and $\Delta E_{ij} = E_i - E_j$ denotes the site energy difference between two neighboring sites, where E_i is the site energy of the ith molecule.

The transfer integrals, or coupling elements, $J_{ij} = \langle \psi_i | \hat{H} | \psi_j \rangle$, characterize the interaction strength between the two frontier orbitals ψ_i and ψ_j on each molecule within a charge transfer complex. These integrals are highly sensitive to both orbital properties and molecular orientations, typically decreasing exponentially as the separation distance increases. For each molecular pair (ij), electronic coupling elements were determined using a projection method,[53,54] applying a 0.7 nm center-of-mass cutoff to define neighboring pairs. Calculations were conducted at the PBE/6-311+G(d,p) level of theory via Gaussian09[32] and the VOTCA package.[29,30] The frozen core approximation was used, focusing on the HOMO and LUMO as the primary contributors to the diabatic states within each dimer.

It is important to note that the semilocal PBE functional, while computationally efficient, underestimates HOMO and LUMO energies due to its 0% asymptotic fraction of exchange, as compared to range-separated functionals that include 100% asymptotic exchange.[55–57] While this limitation is unlikely to affect the trends observed in this study due to systematic error cancellation across the investigated molecules, range-separated functionals would provide more accurate absolute frontier orbital energies. We chose the PBE functional to balance computational efficiency and accuracy for the large-scale calculations required in our multiscale workflow. Future studies aiming for higher accuracy in electronic structure calculations may benefit from employing range-separated functionals, especially for HOMO–LUMO gap predictions.

Our study computed charge carrier mobility using a kinetic Monte Carlo (kMC) approach based on charge transfer rates obtained from the Marcus theory in the high-temperature limit. First, we calculated site energies, electronic couplings, and reorganization energies, which were then used to determine the charge transfer rates. By applying an external electric field of 10^4 V/cm along the x, y, and z directions, we extracted the average carrier velocity $\langle v \rangle$. The mobility (μ) was then determined using the following relation:

$$\mu = \frac{\langle v \rangle}{F}, \quad (7)$$

where F is the magnitude of the applied electric field. The mobility values were computed for different temperatures, with room-temperature mobility obtained via extrapolation. Since we considered transport in three-dimensional amorphous morphologies, the final mobility was determined as the average over all three spatial directions. This method comprehensively evaluates charge transport properties, accounting for anisotropic hopping dynamics in disordered systems. To ensure reliable mobility predictions, a sufficient number of sites were included to achieve a nondispersive transport regime under energetic disorder conditions.[58] This required determining the critical temperature T_c, marking the shift from dispersive to nondispersive transport, as predicted by the Gaussian disorder model. The non-dispersive mobilities were fitted to an empirical temperature-dependent model, allowing room-temperature mobility estimations. All charge transport computations were conducted using VOTCA.[29,30]

III. RESULTS AND DISCUSSION

A. QM analysis

The chemical structures of the studied molecules, along with HOMO-LUMO distributions and electrostatic potential (ESP) maps, are displayed in Fig. 1. Detailed descriptions of these molecular fragments and their designations can be found in the methodology section. The center panel of Fig. 1 presents the frontier molecular orbitals (FMOs), where yellow and blue lobes represent the HOMO and LUMO, respectively. These plots show that the FL and AT units contribute significantly to the frontier molecular orbitals. In contrast, the LB, RB, and HE units play a minimal role in FMO distribution. Specifically, the FL unit tends to be associated with the LUMO, while the AT unit aligns with the HOMO. This observation is likely attributable to the lone pairs of nitrogen and oxygen atoms within these units. At the bottom of Fig. 1, the ESP maps show electron density distribution across the molecules. We examined the potential influence of ESP on molecular stacking. Our analysis suggests that the ESP distributions across different molecule regions contribute to electrostatic complementarity, possibly influencing π-stacking interactions. However, given the dominance of van der Waals and π–π interactions in molecular packing, the ESP variations alone do not significantly alter the preferred stacking configurations. Areas of negative potential, indicated by red lobes, appear around electronegative atoms, particularly oxygen, nitrogen, and fluorine, and also in the FL moiety, while the remaining regions, especially the AT unit and HE unit, display blue lobes, signifying areas of positive potential. The distribution of negative ESP (red lobes) is asymmetrical across the molecules, leading to a net dipole moment, as shown in the ESP plots in Fig. 1. In addition, Fig. 2 presents the average electrostatic potential values along with their corresponding standard deviations (SDs) for the studied molecules.[59,60] No apparent relationship is observed between the average ESP values and their fluctuations across these hole-transport materials. The SD values offer a quantitative measure of the extent of ESP variation within each molecule. Among the set, DN exhibits the lowest degree of fluctuation, whereas DD shows the highest. The computed gas-phase dipole moments, ionization energies, electron affinities, and reorganization energies are summarized in Table I.

Based on the data in Table I, the ionization energies (IE_0) of the compounds range from 5.79 to 6.22 eV. Compound DD exhibits the lowest IE at 5.79 eV, while DF has the highest at 6.22 eV. This IE variation is significant for optimizing energy alignment in optoelectronic applications; lower IE values, such as that of DD, could

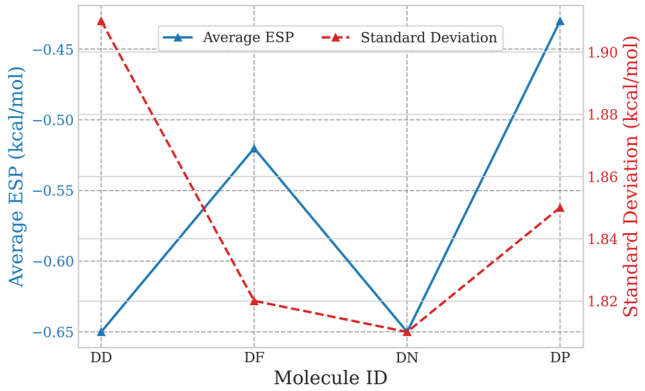

FIG. 2. Comparison of the average electrostatic potential (ESP) values and their standard deviations for four different molecules (DD, DF, DN, and DP). The left *y*-axis (blue) represents the average ESP values (in kcal/mol), while the right *y*-axis (red) shows the corresponding standard deviations. Data points are connected to highlight trends across the molecular systems.

facilitate hole injection when these compounds are used as transport layers, whereas higher IE values, as observed for DF, may offer improved stability when used as host materials. The electron affinities (EA_0) show a relatively narrow range, spanning from 1.25 eV (DP) to 1.37 eV (DF). This slight variation in EA suggests that all compounds have similar affinities for accepting electrons, with DF showing a slight advantage in electron capture. These close EA values imply that the compounds can achieve similar energy level alignment when incorporated into devices like organic light-emitting diodes.

Regarding reorganization energies, the values for electron transfer (λ_e) are higher across all compounds, falling between 0.44 and 0.51 eV. In contrast, the reorganization energies for hole transfer (λ_h) are considerably lower, ranging from 0.14 to 0.27 eV. This distinction indicates that these molecules are more favorable for hole transport, as lower reorganization energies correlate with enhanced charge mobility, particularly for holes. Notably, DD has the lowest λ_h (0.14 eV), suggesting that it may outperform the other compounds in hole transport applications. Finally, the dipole moments (μ^{dip}) show little variability, with values between 3.15 and 3.31 Debye. This uniformity in dipole moments aligns with the consistent ESP map patterns discussed earlier, indicating that these molecules have similar electrostatic distributions, which could contribute to their stability and similar interactions in device environments.

TABLE I. Summary of QM properties: gas-phase ionization energies (IE_0), electron affinities (EA_0), reorganization energies for electron (λ_e) and hole (λ_h) transport in eV, and dipole moments (μ^{dip}) in Debye for each compound.

	DD	DF	DN	DP
IE_0	5.79	6.22	6.10	6.14
EA_0	1.32	1.37	1.28	1.25
λ_e	0.51	0.49	0.44	0.47
λ_h	0.14	0.27	0.20	0.20
μ^{dip}	3.22	3.15	3.31	3.29

B. Amorphous morphologies

The reliability of the generated amorphous morphologies was validated through multiple approaches. First, the distribution of molecular dipole moments obtained from MD-simulated trajectories was examined. The MD-calculated dipole moments were compared with the quantum mechanical dipole moments, and Fig. 3 illustrates this comparison. The QM-calculated dipole moments (indicated by vertical lines) closely align with the peaks of the MD-derived dipole moment distributions, confirming the accuracy of the force field employed. The average dipole moments (μ^{dip}_{avg}) and their standard deviations are presented in Table S1, showing that DD exhibits the highest standard deviation (0.35), indicative of more significant variation over the trajectory, while DP has the lowest standard deviation (0.26), suggesting relatively stable dipole fluctuations. These variations reflect the polarizabilities and dynamic behaviors of the molecules under simulation conditions. In addition, we compared the QM-optimized structures with MD-generated conformations to validate the dihedral potential employed in our approach, demonstrating strong agreement in the dihedral distributions (Fig. S1). We also performed a DFT potential energy scan for the FL-AT unit's single-bond dihedral to verify the accuracy of the Sobtop force field. The results (Fig. S13) show excellent agreement between the DFT-derived potential energy surface and the force field, confirming that our parameterization reliably captures the dihedral flexibility of the system. To further confirm the reliability of the morphologies, density convergence was analyzed, as illustrated in Fig. S2. The system's density stabilized with minimal changes, indicating that equilibrium was achieved without artificial constraints from the initial configuration. These validations collectively confirm that the generated morphologies are well-equilibrated, accurately represent the amorphous phases, and are suitable for subsequent analyses, including calculations of electronic couplings and site energy distributions.

1. Radial distribution functions

To evaluate the packing efficiency of each molecule in the amorphous phase, we divided each molecule into five distinct fragments, allowing a detailed examination of the packing behavior for

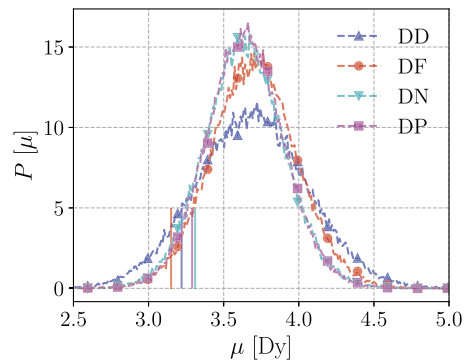

FIG. 3. Distributions of dipole moments from MD simulated trajectories of amorphous HTMs. The solid vertical lines indicate the dipole moment of the isolated molecule obtained from quantum mechanical calculations at the B3LYP/6-311+G(d,p) level of theory, serving as a reference.

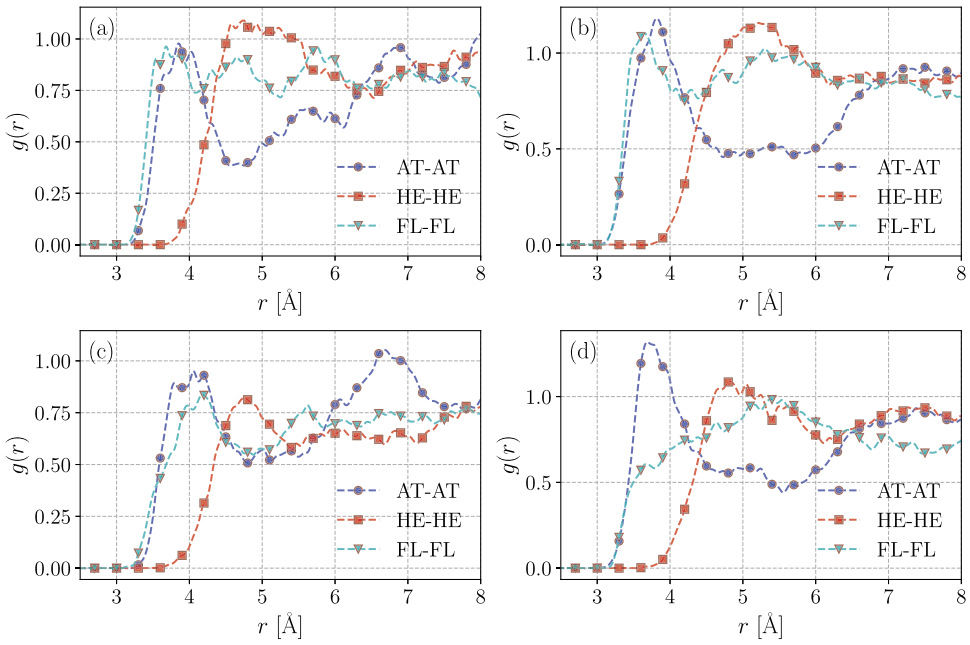

FIG. 4. Radial distribution function plots for selected fragment pairs across the four investigated molecules: (a) DD, (b) DF, (c) DN, and (d) DP.

each fragment individually. Radial distribution functions (RDFs) were then generated for each fragment, considering interactions with the same fragment type and other fragments across neighboring molecules. In this analysis, we focused solely on intermolecular interactions, explicitly assessing the spatial arrangement of fragments from one molecule relative to fragments of other molecules, thereby omitting intramolecular interactions to capture the overall molecular packing better.

Our analysis begins with examining RDFs for identical fragment pairs, shown in Fig. 4, focusing on three key fragments: AT, HE, and FL. The RDF peaks indicate that the intermolecular AT-AT and FL-FL fragment pairs exhibit closer packing distances than the HE-HE pairs, with initial peaks for AT-AT and FL-FL pairs occurring around 4 Å. This closer distance for AT-AT and FL-FL pairs implies stronger packing interactions relative to the HE-HE pairs, except in the DP molecule. In DP, however, the FL-FL peak is broader and exhibits a small shoulder around 4 Å. The initial RDF peaks of AT-AT and FL-FL pairs for the DD compound appear at distances slightly below 4 Å. In contrast, the HE-HE peak is closer to 5 Å, suggesting less efficient packing for HE fragments. The DF compound [Fig. 4(b)] demonstrates similar AT-AT and FL-FL peak positions to DD, indicating enhanced packing efficiency for these fragment pairs in DF. Here, the HE-HE peak shifts slightly, reinforcing its relatively weaker packing contribution. AT-AT and FL-FL peaks shift slightly for the DN molecule, while the HE-HE peak remains within 5 Å, suggesting relatively consistent packing across all fragments.

To further interpret the packing preferences, we observe that the AT and FL fragments, both conjugated rings, likely interact via π-π stacking, leading to higher peak intensities and closer intermolecular distances. These interactions facilitate stronger non-covalent contacts between molecules, enhancing packing efficiency in the amorphous phase. The flexible hexyl chain in the HE fragment, lacking π-π stacking capability, exhibits weaker packing interactions, as evidenced by its broader and more distant RDF peaks. This analysis suggests that the molecules primarily pack through π–π interactions between AT and FL units, where these interactions contribute significantly to the molecular organization and stability of the amorphous structure.

To understand the role of terminal fragments in molecular packing, we conducted RDF analysis on the side fragments, specifically the LB and RB units, as shown in Fig. 5. This analysis is essential because, while the AT, FL, and HE fragments remain consistent across all molecules, the variations in terminals impact packing behavior. Despite LB and RB being distinct moieties within each molecule, they share the same chemical structure within each compound. For instance, in DP, both LB and RB are simple phenyl groups, whereas in DF, they are fluoro-phenyl groups; in DN, they are naphthalene units; and in DD, they consist of N,N,N-triphenyl groups.

From Fig. 5(a), we observe that the first RDF peak height for DD is less than 1. This value, being less than 1, suggests that the local density around the LB and RB fragments is lower than the bulk density, meaning these fragments tend to be more dispersed. This pattern can be attributed to the bulky N,N,N-triphenyl groups, which increase the spatial separation between LB and RB fragments. In DF, the first peak appears around 6 Å, and the RDF profile is more uniform, likely due to the similar nature of the fluoro-phenyl LB and RB units. In DN, the RDF peak shifts slightly past 6 Å, and the profile deviates slightly due to the compact nature of the naphthalene unit, in contrast to the fluoro-phenyl or phenyl groups in DF and DP. The DP molecule, being structurally simpler, shows consistent peak patterns, with peaks appearing at distances of less than 6 Å, indicating a more uniform packing behavior compared to DD and DN.

In summary, as the complexity of the side fragments increases, so does the variability in their packing behavior. Larger side

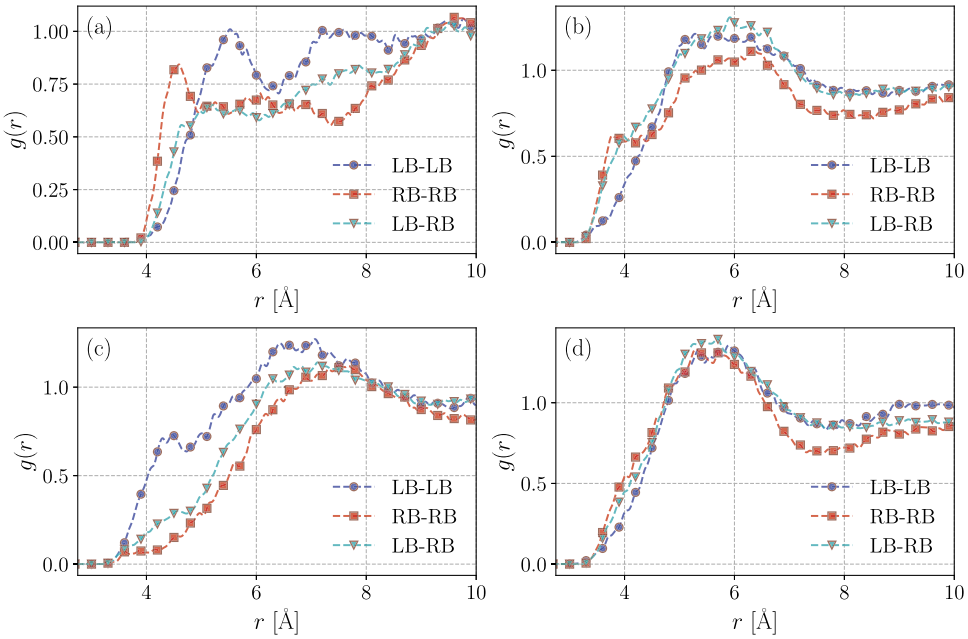

FIG. 5. Radial distribution function plots for selected fragment pairs across the four investigated molecules: (a) DD, (b) DF, (c) DN, and (d) DP.

fragments, such as in DD and DN, tend to be spatially distributed further from each other due to their bulkiness, while simpler fragments, as in DP and DF, allow for more efficient and uniform packing. This trend implies that side fragment size and structure strongly influence molecular packing efficiency, with simpler structures like those in DP facilitating tighter packing than bulkier ones like DD and DN.

To further examine interactions between distinct fragment pairs, we analyzed RDFs for various fragment combinations, presented in Figs. S3 and S4. These plots reveal that all RDF peaks in DD and DN molecules remain below 1, converging to 1 at larger distances. This pattern indicates that the local density for cross interactions between different fragment types is lower than the bulk density within shorter distances (under 5 Å). Interactions between

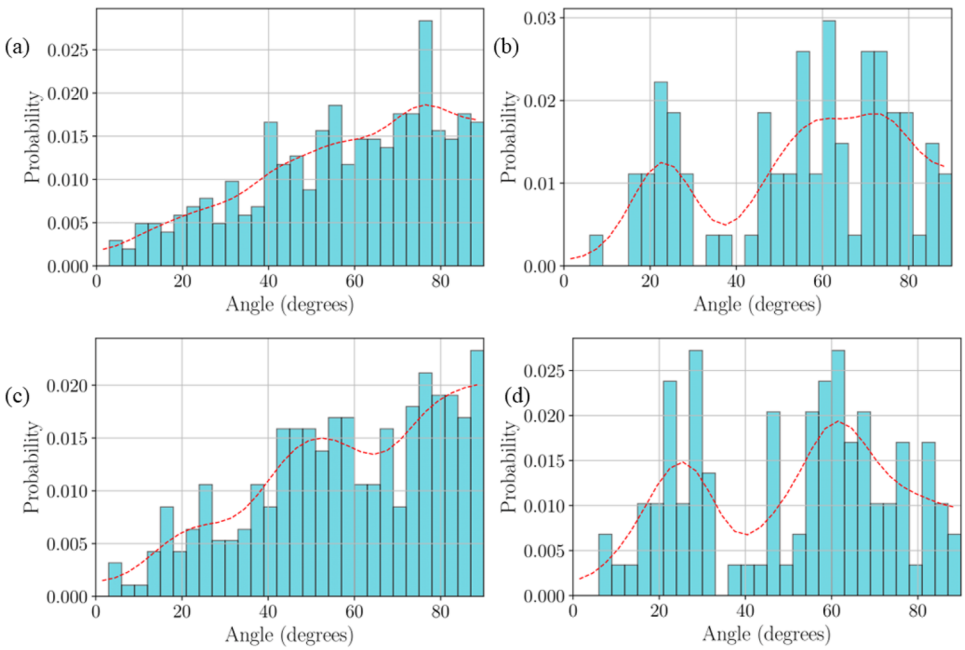

FIG. 6. Angular distribution of principal axes between neighboring molecules within 5 Å, illustrating preferred molecular alignments in the investigated compounds: (a) DD, (b) DF, (c) DN, and (d) DP. Distinct peaks indicate alignment preferences influenced by molecular size and side group sterics.

distinct fragments are less favorable in these molecules than those within identical fragments. For the DP and DF molecules, cross-pair RDF peaks occur at shorter distances due to the smaller molecular size, but even here, the peaks are found at distances exceeding 5 Å. This result suggests that, despite the closer proximity due to molecular size, cross-interactions are still relatively weak and less favored when compared to interactions between identical fragment pairs. These findings have significant implications for our understanding of molecular interactions, highlighting that molecular structure and fragment size play significant roles in determining the preference for interactions within similar fragments over cross-fragment interactions.

2. Principle axis analysis

To gain additional insight into the molecular alignment among neighboring molecules, we defined a principal axis through each molecule's FL and AT units. Using this axis, we calculated the angle between the axes of two adjacent molecules within a 5 Å cutoff. The resulting angle-probability distribution, shown in Fig. 6, highlights distinct alignment patterns. DD molecules exhibit a peak around 80°, indicating a preferred near-orthogonal alignment. DN molecules show a similar distribution, with an angle close to 90° most favored. This preference for orthogonality can be attributed to the bulkier side groups in DD and DN, such as N,N,N-triphenyl and naphthalene, which drive molecules into an orthogonal alignment due to steric repulsion. In contrast, DF and DP molecules display two distinct peaks at ~30° and 60°, suggesting that both parallel and tilted orientations are feasible. This difference is likely due to the smaller side groups in DF and DP, which allow for closer packing and greater flexibility in orientation. Therefore, while steric hindrance in DD and DN limits the range of alignment, the reduced steric constraints in DF and DP enable more varied arrangements.

C. Non-covalent interactions

To further understand the nature of non-covalent interactions among the investigated molecules, we conducted a non-covalent interaction (NCI) index analysis using reduced density gradient plots, as shown in Fig. 7. This approach helps identify and distinguish between attractive, repulsive, and van der Waals interactions through characteristic peaks in the RDG plots. By examining the sign of the second eigenvalue (λ_2) of the electron density Hessian matrix in combination with the electron density (ρ), the interactions can be classified and visualized: sign(λ_2)ρ values near zero signify van der Waals interactions, shown in green; negative values

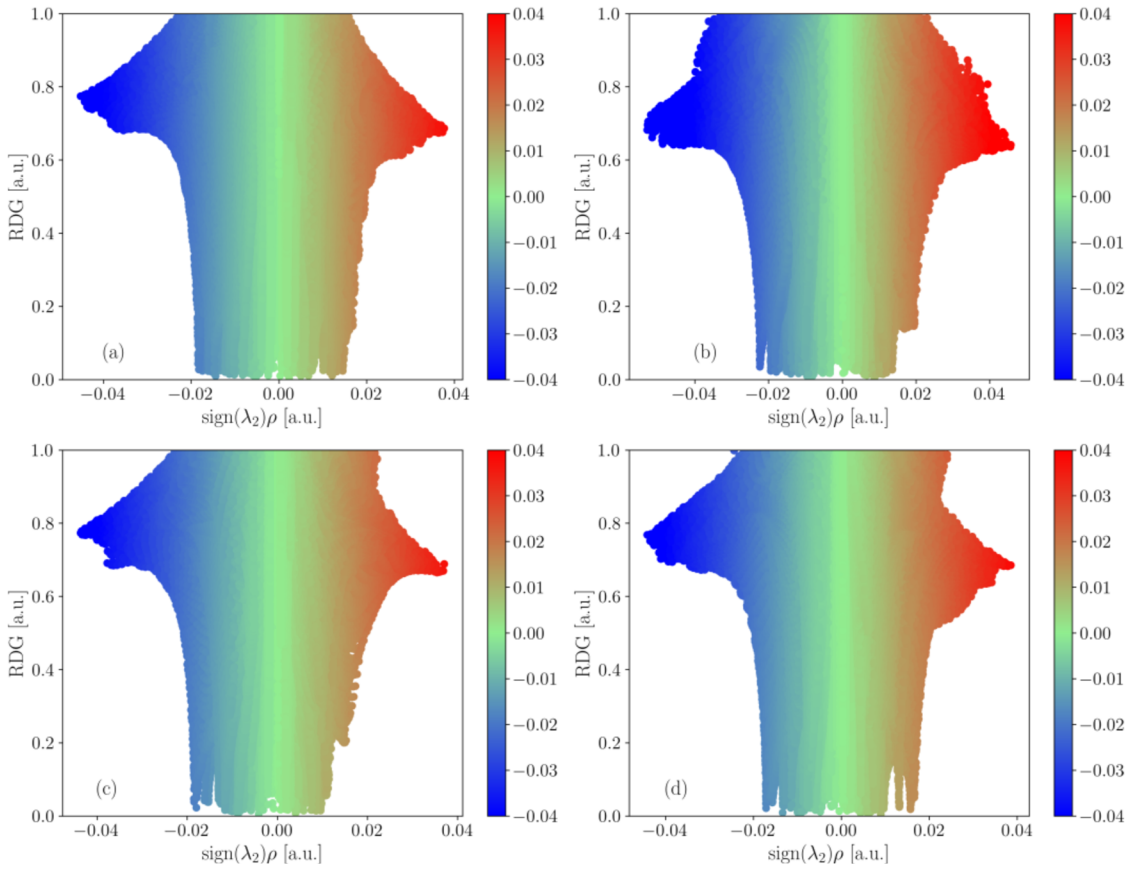

FIG. 7. Reduced gradient density plotted against sign(λ_2)$\rho(r)$ for (a) DD, (b) DF, (c) DN, and (d) DP.

TABLE II. Mean value of integral density in different regions corresponding to NCI analysis.

NCI	Total	Attractive	van der Waals	Steric repulsion
DD	0.0297	0.0082	0.0181	0.0034
DF	0.0291	0.0070	0.0189	0.0032
DN	0.0226	0.0061	0.0138	0.0027
DP	0.0205	0.0055	0.0126	0.0024

$[\mathrm{sign}(\lambda_2)\rho < 0]$ represent attractive interactions, such as hydrogen bonds, shown in blue; and positive values correspond to steric repulsions, visualized in red.

The RDG plots reveal distinct interaction patterns among the molecules. The DP molecule, for example, shows notable van der Waals interaction $[\mathrm{sign}(\lambda_2)\rho \le 0.02]$ with a broader green region indicative of such observation. Peaks for DN appear within a range of −0.01 to 0.01, consistent with stronger van der Waals contributions compared to the other molecules (particularly DD and DF). In contrast, the DF molecule has a narrower van der Waals region, with interactions spanning only from −0.01 to 0.01 and a more prominent steric repulsion peak beyond 0.01, particularly evident in red. The DD molecule shows uniform densities, and there are very few peaks, and the peaks are merged with one another, showing that the interactions are less in this molecule.

A quantitative analysis over a 3 ns trajectory, focusing on the final 38 frames, provides deeper insight into non-covalent interactions (Table II). The integrated values of ρ within the range $[-0.1, 0.1$ a.u.$]$ classify interactions as strong attractive $(-0.1 \le \mathrm{sign}(\lambda_2)\rho < -0.02)$, van der Waals $(-0.02 \le \mathrm{sign}(\lambda_2)\rho \le 0.02)$, and repulsive $(0.02 < \mathrm{sign}(\lambda_2)\rho \le 0.1)$, with higher values indicating weaker overall interactions. These calculations, centered on the molecule's center of mass, account for surrounding atoms within a cutoff distance defined by the first peak in the RDF plots.

The results indicate that the DD molecule, being the largest, has the highest integrated density values across all regions, reflecting weaker non-covalent interactions. This is attributed to its bulkier structure, which reduces the proximity of surrounding atoms. In contrast, the smallest molecule, DP, exhibits the lowest total integrated density, implying stronger non-covalent interactions due to its compact structure, allowing more atoms within the interaction range. The DF and DN molecules occupy intermediate positions, with DN displaying slightly stronger interactions compared to DF, possibly due to differences in molecular substitution patterns. Overall, the trend highlights that molecular size and steric effects significantly influence the strength of non-covalent interactions, with compact molecules like DP promoting stronger attractive and van der Waals interactions, while bulkier molecules like DD exhibit reduced interaction strengths. Detailed ρ values across frames further support these observations, as shown in Figs. S5–S8.

D. Density of states

In the solid state, ionization energies and electron affinities of the four investigated HTM molecules—DD, DF, DN, and DP—reflect fundamental electronic properties influenced by electrostatic and induction effects. To accurately represent solid-state energetics, both the gas-phase IE and EA are adjusted by incorporating electrostatic (E^{ele}) and induction (E^{ind}) contributions, which simulate the environmental polarization and response that a molecule experiences in a condensed phase. This correction is essential because isolated gas-phase values do not account for the collective, field-induced stabilization in solid-state environments. The energetic disorder for holes and electrons was calculated for five independent configurations for each molecule, with values for both holes and electrons summarized in Table S2. Notably, the standard deviation in the energetic disorder is nearly zero in nearly all cases, indicating a high degree of morphological similarity across configurations. For electron disorder, the standard deviation shows maximum fluctuation up to 0.05, while for hole disorder, it was 0.01. These small deviations confirm the uniformity in disorder values, suggesting that any configuration can reliably represent the morphological characteristics for further analysis. Overall, the ionization energies and electron affinities in these investigated molecules are outside the trap-free energy window,[61] implying possible electron trapping in these systems.

Table III shows that the ionization energies range from 4.63 eV for DD to 5.35 eV for DF, highlighting DF as the most resistant to hole injection. Its elevated IE suggests it has greater stability against oxidation, likely due to the presence of fluorine, which increases electron withdrawal and stabilizes the electronic structure. The electron affinities, however, are negative across all molecules, indicating limited electron acceptance ability under solid-state conditions. For instance, DD and DN share the lowest EA values of −0.52 eV, while DF has the least negative EA at −0.40 eV, implying marginally better electron stabilization.

TABLE III. Solid-state ionization potential (IP), induction (E_h^{ind}) and electrostatic (E_h^{ele}) contributions for holes, hole energy disorder (σ_h), solid-state electron affinity (EA), induction (E_e^{ind}) and electrostatic (E_e^{ele}) contributions for electrons, electron energy disorder (σ_e), simulated ($\mu^h_{\mathrm{Sim}} \times 10^{-3}$) and experimental ($\mu^h_{\mathrm{Exp}} \times 10^{-3}$) hole mobility values. Energy values are in eV, and mobility values are in $\mathrm{cm}^2/\mathrm{Vs}$.

Molecule	IP	E_h^{ind}	E_h^{ele}	σ_h	EA	E_e^{ind}	E_e^{ele}	σ_e	μ^h_{Sim}	μ^h_{Exp}
DD	4.63	0.67	0.22	0.15	−0.52	0.60	−0.21	0.24	0.07	5.7
DF	5.35	0.54	0.03	0.15	−0.40	0.64	−0.03	0.18	0.41	4.5
DN	5.00	0.59	0.20	0.15	−0.52	0.63	−0.19	0.20	0.24	4.9
DP	5.00	0.56	0.25	0.16	−0.46	0.66	−0.24	0.20	0.18	6.7

A significant component of these solid-state adjustments arises from induction effects, which are more pronounced than electrostatic contributions. Induction energies (E^{ind}) for both holes and electrons are consistently higher across all molecules, underscoring the polarizability of the solid-state environment as it dynamically responds to the presence of an electron or hole. For instance, the induction energy for electrons in DF is notably high (0.64 eV), indicating strong stabilization due to environmental polarization around an electron. In contrast, DD has the highest induction energy for holes (0.67 eV), hinting that its bulky N,N,N-triphenyl groups may contribute to a more significant polarization response when a hole is introduced. Comparing electrostatic energies (E^{ele}) between holes and electrons, the values indicate a lesser contribution than induction but still support overall stabilization. For example, in DP, the electron electrostatic energy (−0.24 eV) is the most stabilizing among the four, likely due to structural factors that enhance electron localization. The relative balance of these electrostatic and induction contributions is crucial as it determines each molecule's tendency to either donate or accept charge carriers in a solid-state matrix.

The Gaussian disorder model (GDM) provides a framework for understanding charge transport in disordered organic semiconductors by considering the energetic landscape as a Gaussian distribution. In the context of our HTMs, the distributions of solid-state ionization energies and electron affinities follow a Gaussian shape, as shown in Fig. 8. This Gaussian distribution underscores the presence of energetic disorder in the materials, with σ_h and σ_e representing the standard deviations that quantify this disorder for hole and electron transport, respectively. According to GDM, lower energetic disorder—represented by smaller σ values—improves carrier mobility by reducing the likelihood of carriers encountering energetic barriers that can lead to trapping or scattering. As observed in Table III, σ_h values are generally lower than σ_e values across all molecules, indicating that these materials possess a more favorable energy landscape for hole transport, consistent with their function as hole-transport materials. For example, DD, with the lowest σ_h at 0.15 eV, demonstrates a tighter distribution in energy levels that facilitates hole mobility. In contrast, the broader distribution in σ_e, as seen with DD's σ_e = 0.24 eV, aligns with the expected greater disorder in electron transport, reinforcing that these materials are optimized for hole conduction within the Gaussian disorder framework.

E. Couplings and mobility

The determination of the cutoff distance for electronic coupling calculations was guided by the center-of-mass to center-of-mass (COM-COM) RDF. The COM-COM RDF provides a holistic representation of molecular packing, capturing the spatial distribution of entire molecules rather than specific fragments. The COM-COM RDF (see Fig. S9) shows that the first coordination sphere extends up to 7 Å for the representative molecule, DF. Consequently, this distance was chosen as the cutoff for electronic coupling calculations across all studied systems. While fragment-specific RDFs (e.g., AT-AT and FL-FL) indicate strong π–π interactions within a shorter range (~5 Å), the COM-COM RDF accounts for the entire molecular geometry and packing, which extends the interaction range. This approach includes all relevant molecular pairs within the first coordination shell, providing a comprehensive basis for coupling calculations. The electronic coupling elements for both electrons and holes are analyzed in Fig. S10, where the plot of the logarithm of the squared coupling values against their probability reveals a Gaussian-like distribution within this class of molecules. Although the general coupling trends are similar for electrons and holes, slight differences in peak width and height are observable, indicating subtle variations in coupling distributions. In addition, Fig. S14 displays a histogram of the coupling value distributions with the average coupling for each studied molecule.

To gain further insights into how these coupling values relate to charge transfer rates, Fig. 9 shows a plot of the logarithmic coupling values as a function of the intermolecular distances, specifically for hole transport. The corresponding electron transport data is available in Fig. S11. In Fig. 9, we observe that coupling values decrease as the distance between molecular pairs increases, leading to a decline in hole transfer rates at greater distances. This trend is represented by color-coded points, where higher hole transfer rates are indicated by yellow at shorter distances with stronger couplings, while blue represents lower transfer rates at larger distances with weaker couplings.

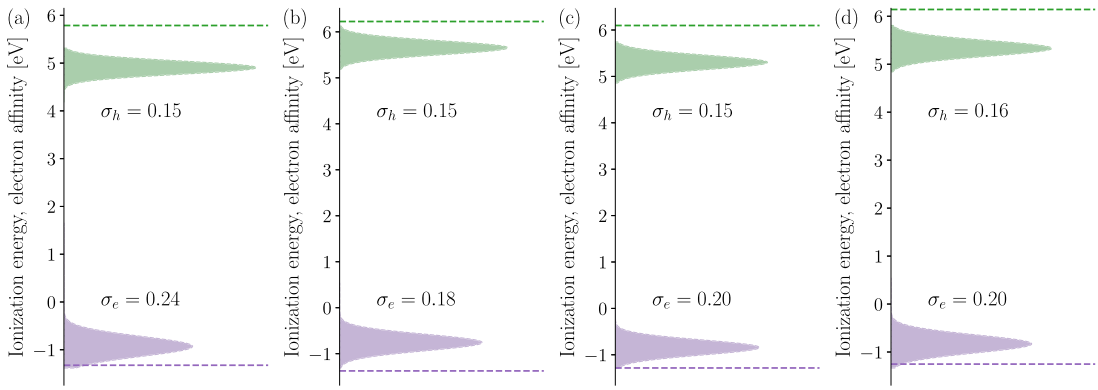

FIG. 8. The density of states (distribution of site energies) in the amorphous materials for anion (shown in purple) and cation (shown in green). Gas-phase ionization energy (IE_0) values obtained by B3LYP/6–311+g(d, p) level of theory are shown using blue dashed lines: (a) DD, (b) DF, (c) DN, and (d) DP.

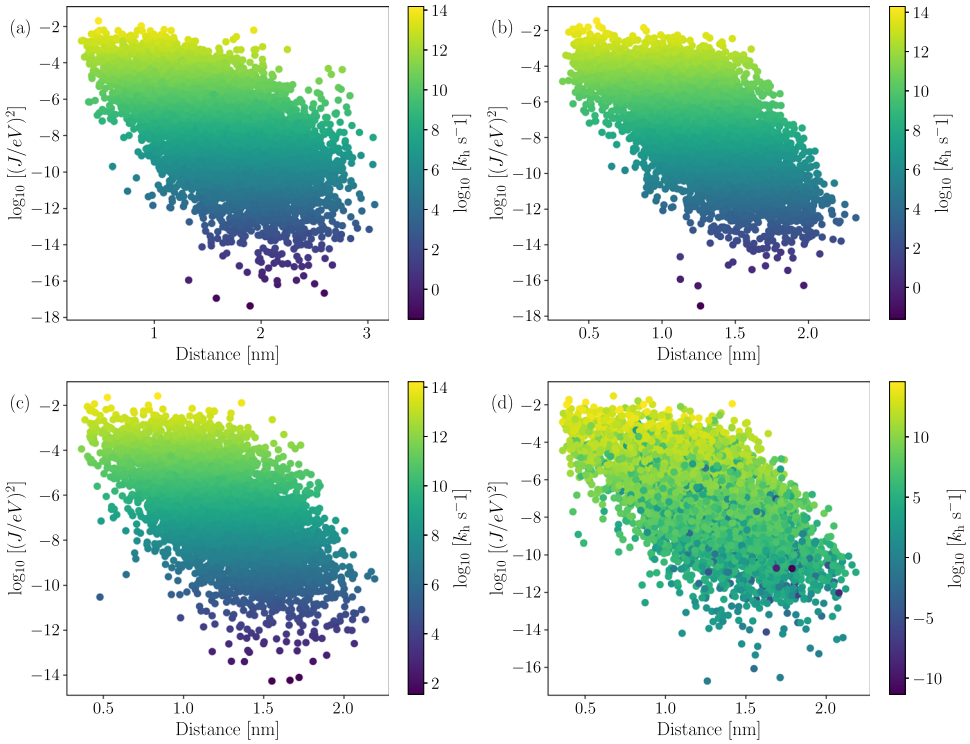

FIG. 9. The coupling values (logarithmic scale) are plotted against intermolecular distances, with color intensity indicating hole transfer rates: yellow represents higher rates at shorter distances with stronger couplings, while blue indicates lower rates at larger distances with weaker couplings: (a) DD, (b) DF, (c) DN, and (d) DP.

In addition, while the coupling values exhibit a similar Gaussian distribution pattern, as shown in Fig. S10, the charge transfer rates deviate due to additional factors. Specifically, the rates are influenced not only by the coupling elements but also by site and reorganization energies, which collectively determine the efficiency of charge transport. This complex dependency emphasizes that strong coupling alone does not guarantee high transfer rates, as other energetic considerations play a crucial role in modulating charge transport across the material.

The energetic disorder significantly impacts the charge carrier mobility, as it follows the relationship $\mu \propto \exp\left[-C\left(\frac{\sigma}{k_B T}\right)^2\right]$. This disorder results from local fluctuations in electronic states, broadening the energy distribution, which aligns with a Gaussian profile as shown in Fig. 8. Using these inputs, mobility was computed based on Eq. (7), applying an electric field of 10^4 V/cm. Notably, a sufficient density of non-dispersive sites is necessary for effective charge transport.[21,62,63] The critical temperature, a factor that influences charge mobility, was computed using the following equation:

$$\left(\frac{\sigma}{k_B T}\right)^2 = -5.7 + 1.05 \ln N, \tag{8}$$

where we assumed $N = 1000$. Table S3 lists the critical temperature values derived from this equation. For temperatures above these critical thresholds, mobilities were evaluated along each principal axis (x, y, and z). The temperature dependence of hole mobilities is shown in Fig. S12, and room-temperature mobility values were extrapolated, yielding values summarized in Table III.

As presented in Table III, the calculated hole mobilities span from 0.07×10^{-3} to 0.41×10^{-3} cm^2/Vs, with DD exhibiting the lowest and DF the highest values. Despite DD exhibiting favorable properties, such as the lowest reorganization and ionization energy, its simulated mobility is the lowest among the studied molecules. This discrepancy arises from the interplay of multiple factors governing charge transport. While lower λ_h and IE facilitate charge transfer, electronic coupling plays a crucial role in determining mobility. As shown in Fig. S14, DD's average coupling is significantly lower than other molecules, directly impacting its charge transport efficiency. In addition, although strong non-covalent interactions generally enhance electronic coupling, our analysis (Table II) indicates that DD exhibits the highest integral density values, typically associated with weaker NCI ability. The lower van der Waals and attractive interaction densities further suggest reduced intermolecular attraction, leading to increased intermolecular spacing and diminished coupling strength. While the triphenylamine end groups can promote intermolecular overlap, their high electron density may also introduce repulsive interactions, further weakening electronic coupling. Although these mobilities are an order of magnitude lower than experimental measurements, they provide valuable insight into the relative charge transport behavior of the studied molecules. The computed electron mobilities (Table S3) are notably smaller than hole mobilities, reinforcing the intrinsic hole-dominated transport characteristics of these materials. These findings highlight the capability of our methodology to capture the underlying structure–property relationships governing charge transport. The discrepancy between simulated and experimental mobility values primarily arises from morphological differences. Our simulations describe an amorphous phase, which is characteristic of device-relevant conditions. In contrast, experimental thin films often exhibit varying degrees of crystallinity, which can lead

to reduced energetic disorder and enhanced charge transport.[20] While a crystalline phase simulation could yield higher mobilities, it would require an experimentally resolved crystal structure, which is currently unavailable. More importantly, our primary objective is to investigate the molecular-level interactions shaping amorphous morphologies and their role in charge transport rather than attempting to precisely match experimental mobility values. Given that OLED device stacks typically incorporate amorphous phases, our simulations provide a relevant framework for understanding charge transport in these materials. Further refinements in morphology representation and rate calculations may improve quantitative agreement with experimental mobilities, but such efforts are beyond the scope of this work.

IV. CONCLUSION

This study investigated four fluorene-based hole-transporting molecules using a multiscale computational approach that integrated quantum mechanical calculations, molecular dynamics simulations, and kinetic Monte Carlo analysis. Through MD simulations, including radial distribution function analysis, principal axis orientation, and non-covalent interaction mapping, we gained crucial insights into molecular interactions that shape amorphous morphologies. RDF analysis revealed a homo-interaction preference, with distinct peaks observed for FL-FL, AT-AT, and LB-LB pairs. At the same time, hetero-fragment interactions were largely absent except for the FL-AT unit. Additionally, principal axis analysis demonstrated that introducing bulky substituents promotes near-perpendicular molecular orientations, as seen in DD. In contrast, with simpler structures, DF and DP exhibited lower-angle orientations of 20° and 60°, respectively.

To refine electronic property predictions, ionization energy, and electron affinity calculations were corrected for induction and electrostatic contributions. The density of states analysis confirmed that all studied molecules have ionization energies within a trap-free window, supporting their suitability as hole transport materials.[61] Charge transfer rates varied among the molecules, with DN exhibiting the highest rates, followed by DD and DF, while DP displayed the lowest. The computed hole mobilities were systematically lower—by an order of magnitude—than experimental values, primarily due to morphological differences. Experimental films tend to exhibit higher crystallinity and lower energetic disorder, enhancing charge transport, whereas our simulations describe the amorphous phase, which is more relevant to OLED device stacks. While crystalline-phase simulations could improve quantitative agreement, our primary focus remains on understanding the molecular interactions governing amorphous morphologies and charge transport. Future work should explore refined morphology representations and disorder effects to bridge simulation and experiment further. In summary, this study highlights the fundamental role of morphology in charge transport and provides a computational framework for the rational design of hole transport materials in optoelectronic applications.

SUPPLEMENTARY MATERIAL

The supplementary material contains tables of average dipole moments, energetic disorders, critical temperatures, density, radial distribution functions, non-covalent interaction parameters, electronic coupling, rates, and mobilities.

ACKNOWLEDGMENTS

The authors gratefully acknowledged the Indian Institute of Technology Gandhinagar, India, for providing research facilities and financial support. Sanyam thanked CSIR for the fellowship. AM acknowledged the SERB (No. SRG/2022/001532) project for funding. They also thanked PARAM Ananta for computational resources.

AUTHOR DECLARATIONS

Conflict of Interest

The authors have no conflicts to disclose.

Author Contributions

Sanyam: Data curation (lead); Formal analysis (equal); Investigation (equal); Methodology (equal); Validation (equal); Visualization (equal); Writing – original draft (equal); Writing – review & editing (equal). **Anirban Mondal**: Conceptualization (lead); Formal analysis (equal); Funding acquisition (lead); Investigation (equal); Methodology (equal); Project administration (lead); Resources (lead); Supervision (lead); Validation (equal); Visualization (equal); Writing – original draft (equal); Writing – review & editing (equal).

DATA AVAILABILITY

The data that support the findings of this study are available from the corresponding author upon reasonable request.

REFERENCES

[1] Y. Shirota and H. Kageyama, "Charge carrier transporting molecular materials and their applications in devices," Chem. Rev. **107**, 953–1010 (2007).
[2] R. A. Belisle, P. Jain, R. Prasanna, T. Leijtens, and M. D. McGehee, "Minimal effect of the hole-transport material ionization potential on the open-circuit voltage of perovskite solar cells," ACS Energy Lett. **1**, 556–560 (2016).
[3] L. Calió, S. Kazim, M. Grätzel, and S. Ahmad, "Hole-transport materials for perovskite solar cells," Angew. Chem. **128**, 14740–14764 (2016).
[4] Y.-H. Kim, L. Weegels, C. Eickhoff, F. May, J. Engelhart, S. Meyer, M. Ricks, and J. Kaiser, "29-3: Improving lateral leakage current in OLED pixels by new hole transport materials: Resolving the crosstalk issue," in *SID Symposium Digest of Technical Papers* (Wiley, 2024), pp. 373–376.
[5] N. B. Kotadiya, H. Lu, A. Mondal, Y. Ie, D. Andrienko, P. W. M. Blom, and G.-J. A. H. Wetzelaer, "Universal strategy for Ohmic hole injection into organic semiconductors with high ionization energies," Nat. Mater. **17**, 329–334 (2018).
[6] U. Würfel, D. Neher, A. Spies, and S. Albrecht, "Impact of charge transport on current–voltage characteristics and power-conversion efficiency of organic solar cells," Nat. Commun. **6**, 6951 (2015).
[7] D. Neher, J. Kniepert, A. Elimelech, and L. J. A. Koster, "A new figure of merit for organic solar cells with transport-limited photocurrents," Sci. Rep. **6**, 24861 (2016).
[8] G. He, M. Pfeiffer, K. Leo, M. Hofmann, J. Birnstock, R. Pudzich, and J. Salbeck, "High-efficiency and low-voltage p-i-n electrophosphorescent organic light-emitting diodes with double-emission layers," Appl. Phys. Lett. **85**, 3911–3913 (2004).

[9]Z. Yang, Z. Mao, Z. Xie, Y. Zhang, S. Liu, J. Zhao, J. Xu, Z. Chi, and M. P. Aldred, "Recent advances in organic thermally activated delayed fluorescence materials," Chem. Soc. Rev. **46**, 915–1016 (2017).
[10]S. Jhulki and J. N. Moorthy, "Small molecular hole-transporting materials (HTMs) in organic light-emitting diodes (OLEDs): Structural diversity and classification," J. Mater. Chem. C **6**, 8280–8325 (2018).
[11]M.-H. Ho, B. Balaganesan, T.-Y. Chu, T.-M. Chen, and C. H. Chen, "A morphologically stable host material for efficient phosphorescent green and red organic light emitting devices," Thin Solid Films **517**, 943–947 (2008).
[12]J. S. Martins, A. A. Bartolomeu, W. H. Dos Santos, L. C. da Silva Filho, E. F. De Oliveira, F. C. Lavarda, A. Cuin, C. Legnani, I. O. Maciel, B. Fragneaud, and W. G. Quirino, "New class of organic hole-transporting materials based on xanthene derivatives for organic electronic applications," J. Phys. Chem. C **121**, 12999–13007 (2017).
[13]X. Cao, D. Zhang, S. Zhang, Y. Tao, and W. Huang, "CN-containing donor–acceptor-type small-molecule materials for thermally activated delayed fluorescence OLEDs," J. Mater. Chem. C **5**, 7699–7714 (2017).
[14]H. Yu, D. Li, H. Bao, Z. Zhang, H. Liu, F. Zhang, and S. Wang, "Multifunctional cross-linked hole transporting interfacial layer for efficient and stable perovskite solar cells," ACS Appl. Energy Mater. **5**, 10742–10750 (2022).
[15]Y. Wu, Z. Gong, Y. Jiang, R. Wang, D. Xu, Z. Xu, G. Zhou, J.-M. Liu, and J. Gao, "Low-cost and efficient hole transport materials based on 9-phenyl-9H-carbazole branch for perovskite solar cells," Surf. Interfaces **28**, 101598 (2022).
[16]V. Joseph, J. Xia, A. A. Sutanto, V. Jankauskas, C. Momblona, B. Ding, K. Rakstys, R. Balasaravanan, C.-H. Pan, J.-S. Ni, S.-L. Yau, M. Sohail, M.-C. Chen, P. J. Dyson, and M. K. Nazeeruddin, "Triarylamine-functionalized imidazolyl-capped bithiophene hole transporting material for cost-effective perovskite solar cells," ACS Appl. Mater. Interfaces **14**, 22053–22060 (2022).
[17]S. Daskeviciute-Geguziene, A. Magomedov, M. Daskeviciene, K. Genevičius, N. Nekrašas, V. Jankauskas, K. Kantminiene, M. D. McGehee, and V. Getautis, "Cross-linkable carbazole-based hole transporting materials for perovskite solar cells," Chem. Commun. **58**, 7495–7498 (2022).
[18]K. Yang, Q. Liao, J. Huang, Z. Zhang, M. Su, Z. Chen, Z. Wu, D. Wang, Z. Lai, H. Y. Woo, Y. Cao, P. Gao, and X. Guo, "Intramolecular noncovalent interaction-enabled dopant-free hole-transporting materials for high-performance inverted perovskite solar cells," Angew. Chem., Int. Ed. **61**, e202113749 (2022).
[19]C. Scherer, N. Kinaret, K.-H. Lin, M. N. Qaisrani, F. Post, F. May, and D. Andrienko, "Predicting molecular ordering in deposited molecular films," Adv. Energy Mater. **14**, 2403124 (2024).
[20]F. H. Hasenburg, K.-H. Lin, B. van der Zee, P. W. M. Blom, D. Andrienko, and G.-J. A. H. Wetzelaer, "Ambipolar charge transport in a non-fullerene acceptor," APL Mater. **11**, 021105 (2023).
[21]A. Mondal, L. Paterson, J. Cho, K.-H. Lin, B. van der Zee, G.-J. A. H. Wetzelaer, A. Stankevych, A. Vakhnin, J.-J. Kim, A. Kadashchuk, P. W. M. Blom, F. May, and D. Andrienko, "Molecular library of OLED host materials—Evaluating the multiscale simulation workflow," Chem. Phys. Rev. **2**, 031304 (2021).
[22]N. B. Kotadiya, A. Mondal, S. Xiong, P. W. M. Blom, D. Andrienko, and G.-J. A. H. Wetzelaer, "Rigorous characterization and predictive modeling of hole transport in amorphous organic semiconductors," Adv. Electron. Mater. **4**, 1800366 (2018).
[23]C. Poelking and D. Andrienko, "Long-range embedding of molecular ions and excitations in a polarizable molecular environment," J. Chem. Theory Comput. **12**, 4516–4523 (2016).
[24]K.-H. Lin, L. Paterson, F. May, and D. Andrienko, "Glass transition temperature prediction of disordered molecular solids," npj Comput. Mater. **7**, 179 (2021).
[25]A. Deniz Özdemir, S. Inanlou, F. Symalla, W. Xie, W. Wenzel, and M. Elstner, "Dynamic effects on hole transport in amorphous organic semiconductors: A combined QM/MM and kMC study," J. Chem. Theory Comput. **19**, 3849–3860 (2023).
[26]G. Kim, "Multiscale calculation of carrier mobility in organic solids through the fine-tuned kinetic Monte Carlo simulation," Comput. Mater. Sci. **218**, 111957 (2023).
[27]H. Sato, S. Kanda, and H. Kaji, "Elucidation of molecular-level charge transport in an organic amorphous system," npj Comput. Mater. **11**, 39 (2025).
[28]A. Madanchi, E. Azek, K. Zongo, L. K. Béland, N. Mousseau, and L. Simine, "Is the future of materials amorphous? Challenges and opportunities in simulations of amorphous materials," ACS Phys. Chem. Au **5**, 3–16 (2024).
[29]V. Rühle, C. Junghans, A. Lukyanov, K. Kremer, and D. Andrienko, "Versatile object-oriented toolkit for coarse-graining applications," J. Chem. Theory Comput. **5**, 3211–3223 (2009).
[30]V. Rühle, A. Lukyanov, F. May, M. Schrader, T. Vehoff, J. Kirkpatrick, B. Baumeier, and D. Andrienko, "Microscopic simulations of charge transport in disordered organic semiconductors," J. Chem. Theory Comput. **7**, 3335–3345 (2011).
[31]M. R. Nagar, A. Choudhury, D. Tavgeniene, R. Beresneviciute, D. Blazevicius, V. Jankauskas, K. Kumar, S. Banik, S. Ghosh, S. Grigalevicius, and J.-H. Jou, "Solution-processable phenothiazine and phenoxazine substituted fluorene cored nanotextured hole transporting materials for achieving high-efficiency OLEDs," J. Mater. Chem. C **10**, 3593–3608 (2022).
[32]M. J. Frisch, G. W. Trucks, H. B. Schlegel, G. E. Scuseria, M. A. Robb, J. R. Cheeseman, G. Scalmani, V. Barone, B. Mennucci, G. A. Petersson, H. Nakatsuji, M. Caricato, X. Li, H. P. Hratchian, A. F. Izmaylov, J. Bloino, G. Zheng, J. L. Sonnenberg, M. Hada, M. Ehara, K. Toyota, R. Fukuda, J. Hasegawa, M. Ishida, T. Nakajima, Y. Honda, O. Kitao, H. Nakai, T. Vreven, J. A. Montgomery, Jr., J. E. Peralta, F. Ogliaro, M. Bearpark, J. J. Heyd, E. Brothers, K. N. Kudin, V. N. Staroverov, R. Kobayashi, J. Normand, K. Raghavachari, A. Rendell, J. C. Burant, S. S. Iyengar, J. Tomasi, M. Cossi, N. Rega, J. M. Millam, M. Klene, J. E. Knox, J. B. Cross, V. Bakken, C. Adamo, J. Jaramillo, R. Gomperts, R. E. Stratmann, O. Yazyev, A. J. Austin, R. Cammi, C. Pomelli, J. W. Ochterski, R. L. Martin, K. Morokuma, V. G. Zakrzewski, G. A. Voth, P. Salvador, J. J. Dannenberg, S. Dapprich, A. D. Daniels, . Farkas, J. B. Foresman, J. V. Ortiz, J. Cioslowski, and D. J. Fox, *GAUSSIAN 09, Revision E.01*, Gaussian, Inc., Wallingford CT, 2009.
[33]T. Lu, Sobtop, Version 1.0, http://sobereva.com/soft.
[34]Q. Shu, F. Yang, Z. Lin, L. Yang, Z. Wang, D. Ye, Z. Dong, P. Huang, and W. Wang, "Molecular understanding of the self-assembly of an N-isopropylacrylamide delivery system for the loading and temperature-dependent release of curcumin," Commun. Chem. **7**, 163 (2024).
[35]Q. Shu, P. Huang, Z. Dong, and W. Wang, "Molecular dynamics investigation on synthesis of a pH- and temperature-sensitive carbon nanotube loaded with doxorubicin," Iscience **27**, 108812 (2024).
[36]S. Liu, H. Wang, J. Yang, S. Luo, Y. Liu, W. Huang, J. Hu, G. Xu, and Z. Min, "Force field benchmark of asphalt materials: Density, viscosity, glass transition temperature, diffusion coefficient, cohesive energy density and molecular structures," J. Mol. Liq. **398**, 124166 (2024).
[37]T. A. Manz and D. S. Sholl, "Chemically meaningful atomic charges that reproduce the electrostatic potential in periodic and nonperiodic materials," J. Chem. Theory Comput. **6**, 2455–2468 (2010).
[38]B. Hess, C. Kutzner, D. Van Der Spoel, and E. Lindahl, "GROMACS 4: Algorithms for highly efficient, load-balanced, and scalable molecular simulation," J. Chem. Theory Comput. **4**, 435–447 (2008).
[39]S. Pronk, S. Páll, R. Schulz, P. Larsson, P. Bjelkmar, R. Apostolov, M. R. Shirts, J. C. Smith, P. M. Kasson, D. Van Der Spoel, B. Hess, and E. Lindahl, "GROMACS 4.5: A high-throughput and highly parallel open source molecular simulation toolkit," Bioinformatics **29**, 845–854 (2013).
[40]L. Martínez, R. Andrade, E. G. Birgin, and J. M. Martínez, "Packmol: A package for building initial configurations for molecular dynamics simulations," J. Comput. Chem. **30**, 2157–2164 (2009).
[41]G. Bussi, D. Donadio, and M. Parrinello, "Canonical sampling through velocity rescaling," J. Chem. Phys. **126**, 014101 (2007).
[42]H. J. C. Berendsen, J. P. M. Postma, W. F. Van Gunsteren, A. DiNola, and J. R. Haak, "Molecular dynamics with coupling to an external bath," J. Chem. Phys. **81**, 3684–3690 (1984).
[43]U. Essmann, L. Perera, M. L. Berkowitz, T. Darden, H. Lee, and L. G. Pedersen, "A smooth particle mesh Ewald method," J. Chem. Phys. **103**, 8577–8593 (1995).
[44]W. Humphrey, A. Dalke, and K. Schulten, "VMD: Visual molecular dynamics," J. Mol. Graphics **14**, 33–38 (1996).
[45]R. A. Boto, F. Peccati, R. Laplaza, C. Quan, A. Carbone, J.-P. Piquemal, Y. Maday, and J. Contreras-García, "NCIPLOT4: Fast, robust, and quantitative analysis of noncovalent interactions," J. Chem. Theory Comput. **16**, 4150–4158 (2020).

[46]R. Sewak, R. Khatua, and A. Mondal, "Non-covalent interactions in conjugated polymer blends: Insights into the stability of PVC/PM6 and CPE/PM6 systems," J. Chem. Phys. **161**, 214902 (2024).
[47]A. J. Stone, "Distributed multipole analysis: Stability for large basis sets," J. Chem. Theory Comput. **1**, 1128–1132 (2005).
[48]P. T. Van Duijnen and M. Swart, "Molecular and atomic polarizabilities: Thole's model revisited," J. Phys. Chem. A **102**, 2399–2407 (1998).
[49]B. T. Thole, "Molecular polarizabilities calculated with a modified dipole interaction," Chem. Phys. **59**, 341–350 (1981).
[50]R. A. Marcus, "Chemical and electrochemical electron-transfer theory," Annu. Rev. Phys. Chem. **15**, 155–196 (1964).
[51]R. A. Marcus and N. Sutin, "Electron transfers in chemistry and biology," Biochim. Biophys. Acta, Rev. Bioenerg. **811**, 265–322 (1985).
[52]R. A. Marcus, "Electron transfer reactions in chemistry: Theory and experiment (Nobel lecture)," Angew Chem. Int. Ed. Engl. **32**, 1111–1121 (1993).
[53]E. F. Valeev, V. Coropceanu, D. A. da Silva Filho, S. Salman, and J.-L. Brédas, "Effect of electronic polarization on charge-transport parameters in molecular organic semiconductors," J. Am. Chem. Soc. **128**, 9882–9886 (2006).
[54]B. Baumeier, J. Kirkpatrick, and D. Andrienko, "Density-functional based determination of intermolecular charge transfer properties for large-scale morphologies," Phys. Chem. Chem. Phys. **12**, 11103–11113 (2010).
[55]L. Kronik, T. Stein, S. Refaely-Abramson, and R. Baer, "Excitation gaps of finite-sized systems from optimally tuned range-separated hybrid functionals," J. Chem. Theory Comput. **8**, 1515–1531 (2012).
[56]M. E. Foster and B. M. Wong, "Nonempirically tuned range-separated DFT accurately predicts both fundamental and excitation gaps in DNA and RNA nucleobases," J. Chem. Theory Comput. **8**, 2682–2687 (2012).
[57]B. M. Wong and T. H. Hsieh, "Optoelectronic and excitonic properties of oligoacenes: Substantial improvements from range-separated time-dependent density functional theory," J. Chem. Theory Comput. **6**, 3704–3712 (2010).
[58]R. Schmechel, "Gaussian disorder model for high carrier densities: Theoretical aspects and application to experiments," Phys. Rev. B **66**, 235206 (2002).
[59]G. Wang, J. Wang, Y. Cui, Z. Chen, W. Wang, Y. Yu, T. Zhang, L. Ma, Y. Xiao, J. Qiao, Y. Xu, X.-T. Hao, and J. Hou, "Achieving high fill factor in organic photovoltaic cells by tuning molecular electrostatic potential fluctuation," Angew. Chem., Int. Ed. **63**, e202401066 (2024).
[60]X. Xie, Z. Chen, and S. Zheng, "Theoretical exploration of the effects of conjugated side chains on the photoelectric properties of Y6-based nonfullerene acceptors," J. Phys. Chem. A **129**, 2866–2875 (2025).
[61]N. B. Kotadiya, A. Mondal, P. W. M. Blom, D. Andrienko, and G.-J. A. H. Wetzelaer, "A window to trap-free charge transport in organic semiconducting thin films," Nat. Mater. **18**, 1182–1186 (2019).
[62]A. Lukyanov and D. Andrienko, "Extracting nondispersive charge carrier mobilities of organic semiconductors from simulations of small systems," Phys. Rev. B **82**, 193202 (2010).
[63]P. Kordt, T. Speck, and D. Andrienko, "Finite-size scaling of charge carrier mobility in disordered organic semiconductors," Phys. Rev. B **94**, 014208 (2016).